AGAP duplicons associate with structural diversity at Chromosome 10q11.22

Stefania Fornezza[1,4], Vincenza Simona Delvecchio[1,4], William T. Harvey[2], Philip C. Dishuck[2], Evan E. Eichler[2,3], Giuliana Giannuzzi[1]*

1. Department of Biosciences, University of Milan, Milan, Italy
2. Department of Genome Sciences, University of Washington School of Medicine, Seattle, WA, USA
3. Howard Hughes Medical Institute, University of Washington, Seattle, WA, USA
4. These authors contributed equally to this work.

* Corresponding author: giuliana.giannuzzi@unimi.it

Running title: 10q11.22 structural variation and *AGAP* duplicons

Keywords: 10q11.22 chromosomal region, *AGAP* genes, segmental duplications, non-allelic homologous recombination, structural variation

Abstract

The 10q11.22 chromosomal region is a duplication-rich interval of the human genome and one of the last to be fully assembled. It carries copy-number variable genes associated with intellectual disability, bipolar disorder, and obesity. In this study, we characterized the structural diversity at this locus by analyzing 64 haploid assemblies produced by the Human Pangenome Reference Consortium. We identified eleven alternative haplotypes that differ in the copy number and/or orientation of large genomic segments, ranging from hundreds of kilobase pairs (kbp) to over one megabase pair (Mbp). We uncovered a 2.4 Mbp size difference between the shortest and longest haplotypes. Breakpoint analysis revealed that genomic instability results from non-allelic homologous recombination between segmental duplication (SD) pairs with varying similarity (94.4–99.6%). Nonetheless, these pairs generally recombine at positions where their identity is higher (>99.6%). Recurrent inversions occur with different breakpoints within the same inverted SD pair. Inversion polymorphisms shuffle the entire SD arrangement, creating new predispositions to copy-number variations. The SD architecture is associated with a catarrhine-specific subgroup of the *AGAP* gene family, which likely triggered the accumulation of SDs at this locus over the past 25 million years of human evolution. Our results reveal extensive structural diversity and genomic instability at the 10q11.22 locus and expand the general understanding of the mutational mechanisms behind SD-mediated rearrangements.

Supplemental material is available for this article.

Introduction

The human genome and the genomes of African apes show an enrichment of large, recent, and interspersed segmental duplications (SDs) (Marques-Bonet et al. 2009). These duplications are not evenly distributed along chromosomes but are clustered at some loci, especially pericentromeric and subtelomeric regions (Bailey et al. 2001; Giannuzzi et al. 2014). SD clusters exhibit a mosaic and complex arrangement due to the duplication of multiple segments from various regions at different times. Within these clusters, a high-copy ancestral "core duplicon" can be identified (Jiang et al. 2007). Genomic intervals with SDs are generally structurally polymorphic because of copy-number variation and inversion of some segments. They also show extensive reorganization when the human sequence is compared to the one at orthologous locations in nonhuman primate genomes (Bailey and Eichler 2006; Antonacci et al. 2014; Nuttle et al. 2016). In fact, due to the high identity between copies, SDs are substrates for non-allelic homologous recombination (NAHR) that generates structural changes of the SDs themselves as well as of the flanking unique regions (Carvalho and Lupski 2016).

Given their impact on genetic diversity, these genomic intervals are expected to significantly influence phenotypic variation and susceptibility to common diseases. While their role in predisposing to pathogenic recurrent deletions and duplications is well established (Bailey et al. 2002; Stankiewicz and Lupski 2002; Migliavacca et al. 2015), their contribution to trait variation remains largely unexplored due to limited knowledge of their diverse structures and challenges associated with genotyping. The recent development of long-read sequencing platforms and new assembly algorithms has enhanced our ability to obtain their sequences and holds promise for overcoming these limitations (Vollger et al. 2019).

The 10q11.22 chromosomal region is one of these complex intervals of the human genome (Chaisson et al. 2015). It has an euchromatic gap in the GRCh38 human reference that derives from the incomplete assembly of a pair of SDs. The gap, which includes *GPRIN2B*, has been resolved by using long reads (Vollger et al. 2019) and a contiguous sequence of the region is available from the T2T (Telomere-to-Telomere) CHM13 human genome sequence (Nurk et al. 2022). The architecture of this locus is the result of several structural changes occurred in the human lineage after divergence with the chimpanzee (Dennis et al. 2017).

Previous works showed that genes mapped on this interval, like *GPRIN2* and *NPY4R*, are copy-number polymorphic (Handsaker et al. 2015; Vollger et al. 2019) and additional *GPRIN2* copies derive from tandem duplications (Liao et al. 2023). 10q11.22 copy-number variation has been associated with obesity (Sha et al. 2009; Jarick et al. 2011; Aerts et al. 2016; Shebanits et al. 2018) and bipolar disorder (Priebe et al. 2012; Chen et al. 2016), while the association with intellectual disability (Cooper et al. 2011; Stankiewicz et al. 2012) was not confirmed in a subsequent study that used a larger cohort (Coe et al. 2014).

In this study, we sought to characterize structural variation at Chromosome 10q11.22 region and gain insights into the molecular mechanisms of its genomic instability.

Results

Duplicon and gene annotation at Chromosome 10q11.22 in the T2T-CHM13 assembly

We assessed SDs, protein-coding genes, and pseudogenes annotated at Chr10:46,500,000-49,100,000 in the T2T-CHM13 genome assembly, as this is the only human reference having a contiguous and gapless sequence of the interval. Overall, 60% of the sequence is composed of SDs (**Fig. 1A**). We underline the presence of three SD pairs exhibiting inverted orientation and high sequence similarity (>99%): a 460 kbp pair containing the *NPY4R/R2*, *GPRIN2A/2B*, *SYT15/15B* protein-coding genes and overlapping the *NPY4R-A* and *NPY4R-B* segments; a 122 kbp pair containing the *PTPN20* gene (designated as *PTPN20-A* and *PTPN20-B* segments); a 68 kbp pair containing the *ANXA8* and *ANXA8L1* genes (designated as *ANXA8-A* and *ANXA8-B* segments) (**Fig. 1A**).

Classification of diverse 10q11.22 structural haplotypes

We leveraged available *de novo* assembled and phased genomes to characterize and catalogue large-scale (> 50 kbp) structural variation at Chromosome 10q11.22. We first assessed which combination of sequencing technology and algorithm better performed in the phased assembly of this locus. We analyzed available sequences of the HG002 and HG00733 genomes that were obtained by using the HiFi (High Fidelity) PacBio (Pacific Biosciences) and/or Nanopore long-read sequencing technologies and the Hifiasm, HiCanu, and/or Shasta tools (Shafin et al. 2020; Cheng et al. 2021). This comparison showed that the PacBio HiFi technology combined with the Hifiasm algorithm produced a contiguous sequence in one out of four haplotypes and had a better performance compared to the other tools that never succeeded in the assembly.

Next, we analyzed our region of interest in diploid and phased assemblies for 47 samples (94 haplotypes) produced by the Human Pangenome Reference Consortium (Liao et al. 2023). These assemblies were produced with the Trio-Hifiasm assembly tool that uses PacBio HiFi long-read sequences and parental Illumina short-read sequences. The locus is assembled in a single contig in 64/94 (68%) genomes. Of these 64 sequences, 49 (77%) have the same structure as T2T-CHM13, which turns out to be the most common haplotype (H1), while 15 sequences have a different structure (**Fig. 1B**). Specifically, eight sequences (8/64 = 12%; haplotypes H2, H9, H10, and H11) display an inversion of the region between the *NPY4R* duplicons, hereby referred to as the *GDF10* segment, which includes the *PTPN20-A* duplicon (**Fig. 1A, B**). This inversion polymorphism was previously described and shown to be a case of mutational toggling (Porubsky et al. 2020; Porubsky et al. 2022). Five haplotypes exhibit expansions (H4, H6, H7) or contractions (H10 and H11) in either the proximal or distal copy of the *NPY4R* segment. We noted that while *ANXA8-A* segment overlaps with the beginning of the *NPY4R-A* segment, *ANXA8-B* is located outside the *NPY4R-B* segment and overlaps the end of the *GDF10* segment susceptible to inversion (**Fig. 1A**). H5 variant shows a tandem duplication of the *ANTXRL* and *NPY4R* segments. We observed another structure (H3) in two assemblies that has a ~170 kbp deletion overlapping the *ANTXRL* segment (**Fig. 1A, B**).

Overall, we identified eleven different structures of the 10q11.22 region, with the T2T-CHM13 configuration being the most prevalent. H2, H3, H5, H9, H10, and H11 haplotypes were also validated by GAVISUNK (Genome Assembly Validation via Inter-SUNK distances in nanopore reads) (Dishuck et al. 2023) using ONT (Oxford Nanopore Technologies) reads from the same samples. H8 was not assessed, while H4, H6, and H7 structures could not be validated due to insufficient ONT coverage across the region.

Copy-number estimates of 10q11.22 genes

We sought to validate the identified diverse structures using another orthogonal approach. We assessed Illumina read-based copy-number estimates of 10q11.22 genes that map to copy-number variant segments, i.e. *ANTXRL*, *NPY4R*, *GPRIN2*, *SYT15*, *NPY4R2, SYT15B, PTPN20, ANXA8*, and *ANXA8L1*, as well as of *AGAP* (ArfGAP with GTPase domain, ankyrin repeat and PH domain) genes (**Fig. 1A**, **Table 1**). We applied both the WSSD (Whole-genome Shotgun Sequence Detection) and SUNK (Singly Unique Nucleotide *K*-mers) methods in 3,436 humans from 1KGP (1000 Genomes Project) and HGDP (Human

Genome Diversity Project) panels, and 57 nonhuman primates. The WSSD method estimates the total copy number for sequences ≥ 95% identity and over 1 kbp, while the SUNK method estimates paralog-specific copy number.

NPY4R, *GPRIN2*, *SYT15*, *NPY4R2,* and *SYT15B* WSSD copy-number plots looked highly similar, with copy numbers ranging from 2 to 8. Most humans carry four diploid copies, while all nonhuman primates have two diploid copies (the *GPRIN2* plot is depicted in **Fig. 2A** as representative). Consistently, human values have high pairwise correlations ($0.59 \leq \rho \leq 1$, $P < 2.2 \times 10^{-16}$) (**Fig. 2B**). These data are in line with our results showing that i) H1 with two copies of the *NPY4R* duplicon is the most common structure and ii) *GPRIN2A*, *NPY4R*, and *SYT15* as well as *GPRIN2B*, *NPY4R2*, and *SYT15B* are located within the same duplicon and are jointly duplicated or deleted.

ANXA8 and *ANXA8L1* WSSD copy numbers were significantly correlated with copy numbers of *NPY4R* duplicon genes ($0.43 \leq \rho \leq 0.48$, $P < 2.2 \times 10^{-16}$) (**Fig. 2B**). This is in line with the location of *ANXA8L1* in the proximal *NPY4R-A* segment. *ANXA8* is duplicated also in African apes (**Fig. 2A**).

We next weighed the *ANTXRL* copy number and used SUNK-based estimates, as WSSD ones seemed to be influenced by the presence of the *ANTXRLP1* pseudogene, whose genomic sequence has a 92% similarity with that of *ANTXRL* (**Fig. 1A**). *ANTXRL* SUNK estimates showed that most humans (3,209/3,436, 93%) and all nonhuman primates have two diploid copies. This gene is copy-number polymorphic, with copy number ranging from 1 to 6 and ~6% of humans (197/3,436) carrying one additional copy (CN = 3) (**Fig. 2A**). *ANTXRL* copy number is moderately correlated with the copy number of genes located within the *NPY4R* duplicon ($0.24 \leq \rho \leq 0.26$, $P < 2.2 \times 10^{-16}$) (**Fig. 2B**). 205/214 (96%) of humans carrying more than two *ANTXRL* copies also carry more than four *GPRIN2* copies. This is in line with the structure of H5, H6, and H7 haplotypes presenting a joint duplication of *ANTXRL* and

NPY4R segments. The lower correlations of *ANTXRL* with genes mapped to the *NPY4R* segment compared to the correlations of genes within the *NPY4R* segment are consistent with our haplotype scheme, in which the *NPY4R* segment varies in its copy number either alone or in concert with the *ANTXRL* segment.

PTPN20 copy number is also variable and moderately correlated with the copy number of genes in the *NPY4R* segment ($0.20 \leq \rho \leq 0.27$, $P < 2.2 \times 10^{-16}$) (**Fig. 2A, B**). This is consistent with the H11 structure that carries a deletion of the *NPY4R-B* segment as well as one less copy of the *PTPN20* segment.

In 3421/3,436 humans, *AGAP1*, *AGAP2*, and *AGAP3*, which map outside Chromosome 10, are in single copy. Conversely, the other ten *AGAP* genes, which map on Chromosome 10, have a WSSD diploid copy number ranging from 15 to 32, with the mean value equal to 19 or 20 (representative *AGAP4* copy-number plot and correlations are shown in **Fig. 2**). In fact, as these ten *AGAP* copies share an identity in their genomic sequence ranging from 97.5 to 99.6% (**Supplemental Table S1**) and the WSSD method considers a 95% identity threshold, the estimates for each gene reflect the diploid copy number of all ten copies together. In line with this, WSSD estimates of Chromosome 10 *AGAP* genes show high pairwise correlations ($0.65 \leq \rho \leq 0.94$, $P < 2.2 \times 10^{-16}$). The copy number of Chromosome 10 *AGAP* genes also correlates with the copy number of the other 10q11.22 genes assessed (**Fig. 2B**). This is in line with the concomitant copy-number variation of *AGAP7P*, *AGAP14P*, *AGAP13P*, *AGAP9*, and/or *AGAP12P* with the other 10q11.22 genes (**Fig. 1B**).

Next, we checked copy-number estimates in 15 samples that are homozygous for the H1 haplotype. *NPY4R*, *GPRIN2*, *SYT15*, *NPY4R2,* and *SYT15B* WSSD estimates, *ANTXRL* and *AGAP10P* SUNK estimates, and *PTPN20* WSSD and SUNK estimates are fully consistent with expected values. *ANXA8* and *ANXA8L1* WSSD estimates correspond to expected values except for one sample. *AGAP* WSSD estimates range from 17 to 20 (predicted value of 20, considering ten *AGAP* copies on each Chromosome 10). SUNK estimates for the *NPY4R/R2*, *SYT15/15B*, *ANXA8/ANXA8L1*, and *AGAP* paralogs do not always coincide with the expectation of two copies (**Supplemental Table S2**).

We evaluated copy-number estimates in samples carrying alternative haplotypes (from H2 to H11) (**Table 2, Supplemental Table S2**). *ANTXRL* SUNK estimates align with its duplication in H5, H6, and H7 haplotypes. Similarly, *NPY4R*, *GPRIN2*, *NPY4R2*, *SYT15B*, and *ANXA8L1* WSSD estimates correspond to the expected values and are consistent with the duplication of the *NPY4R* segment in H4, H5, and H6 haplotypes, as well as the deletion in H10. *AGAP* WSSD estimates usually do not match expectations; however, the general trend aligns with a higher or lower copy number compared to H1-H1 genomes. *NPY4R*, *NPY4R2*, *SYT15*, and *SYT15B* SUNK estimates do not generally align with expectations. Overall, copy-number data support the polymorphic structural configurations that we identified at Chromosome 10q11.22 region.

Lastly, we considered copy-number data of samples with unassembled haplotypes to evaluate whether fragmented sequences correspond to more complex and longer structures with further expansions of these segments. In particular, we retrieved data of samples with one H1 haplotype and the other haplotype unassembled (n = 10) and of samples with both haplotypes unassembled (n = 9). Copy-number data were available for 5 out of 10 and 4 out of 9 samples, respectively, corresponding to an H1-H1 genotype. This suggests that the assembled haplotypes provide an unbiased sample of the large-scale structural variation occurring at Chromosome 10q11.22. It also implies that difficulties in assembling this interval in some samples are not caused by the presence of a high copy-number of these large segments.

Refinement of structural variation breakpoints

To gain insights into the mechanism originating 10q11.22 structural diversity, we sought to i) identify the location of the variant breakpoints; ii) narrow down as much as possible the interval; iii) assess sequence features at the refined locations. We considered the alternative haplotypes that were validated by GAVISUNK and assumed that the H1 haplotype, the most common one, is the parental structure from which new haplotypes were formed.

As we noted that all variant breakpoints map to SD clusters, we posited that the new haplotypes were generated by SD-mediated NAHR. As recombination activity is higher in females than in males at this locus, we infer that most 10q11.22 NAHR events might occur during maternal meiosis (**Supplemental Fig. S1**). Precisely, interchromosomal or interchromatidal NAHR between SDs with direct orientation can generate alleles with the duplication or deletion of the intervening sequence together with the gain or loss of one SD copy (**Fig. 3A**). Additionally, the new SD copy or the remaining one are "chimeras," with the first portion derived from the downstream SD copy and the second part derived from the upstream SD copy in the duplication allele, and vice versa in the deletion allele (**Fig. 3A**). Similarly, intrachromatidal NAHR between SDs with inverted orientation can generate alleles with inversion of the segment in-between. The inversion also reshuffles the flanking SDs and mutate them to two hybrid copies (**Fig. 3A**). The junction between the two parts derived from the original SD sequences corresponds to the exact NAHR breakpoint.

We first identified the SD pair that putatively underlies the NAHR event at the origin of the variant. Next, we conducted a sliding window diversity analysis, comparing the SD hybrid sequence/s (one in case of deletion or duplication and two in case of inversion) with each parental SD sequence from the T2T genome assembly ("A" and "B" duplicons). Additionally, we assessed the diversity between the two parental SD sequences as a reference. We visually examined the resulting patterns to identify the position where the derived hybrid SD sequence transitions from being a better match to one SD of the pair to being a better match to the other

SD of the same pair. Finally, the breakpoint corresponds to the entire interval at the switch that cannot be confidently assigned to either parental SD.

SDs generating the deletion in the H3 allele belong to clusters containing *AGAP7* and *AGAP14* copies, while those that underlie the joint duplication of *ANTXRL* and *NPY4R* segments in the H5 allele encompass, respectively, *AGAP7* and *AGAP13* copies (**Fig. 1A, B**). We refined the breakpoints of H3 deletion and H5 duplication to, respectively, 369 and 867 bp intervals with perfect identity and no genes annotated (**Fig. 3B, Table 3, Supplemental Fig. S2 and S3, Supplemental Table S3**). While the first interval is characterized by a high GC content (66%), the second one corresponds to a LINE (Long Interspersed Nuclear Element) (**Table 3, Supplemental Fig. S2 and S3**).

We next analyzed the five different haploid genomes corresponding to the H2 haplotype with inversion of the *GDF10* segment. This inversion is mediated by inverted copies of *NPY4R* duplicons (**Fig. 1A**). We compared the sequence of the parental duplicons with that of the derived hybrid duplicons at both sides of the inversion from H2 genomes (**Supplemental Fig. S4A**). As the breakpoint region was consistent between the two approaches (analysis of "AB" and "BA (reverse complement)" duplicons), we considered the intersection between the two breakpoint intervals as the final breakpoint (**Table 3**, **Supplemental Table S3**). We found that the five H2 inverted chromosomes derive from five distinct inversion events with different breakpoints (**Supplemental Fig. S4)**. We observed that H2.3-BA, H2.4-BA, and H2.5-AB plots show unforeseen intervals where the duplicon switches again its higher similarity from the "A" copy (blue line) to the "B" copy (red line) (**Supplemental Fig. S4A**).

Our analysis of the H9 haplotype with inversion of a region that includes both the *GDF10* segment and the *NPY4R-A* duplicon showed that this rearrangement was mediated by inverted copies of *ANXA8* duplicons and the breakpoints occur at *ANXA8* loci (**Fig. 3C, Table 3, Supplemental Fig. S5, Supplemental Table S3**). Breakpoint analysis of H11 and H10 haplotypes, respectively with the deletion of the distal and proximal copy of the *NPY4R* duplicon, showed that they likely derived, respectively, from the H2 and H9 inverted haplotypes. In fact, the inversion in H2 changes the reciprocal orientation of *PTPN20* duplicons from indirect to direct and these can thus mediate the H11 deletion (**Fig. 4A**). Similarly, the inversion in H9 changes the reciprocal orientation of *NPY4R* duplicons from indirect to direct and locates them in a tandem configuration. This new configuration is susceptible to the deletion of one copy of *NPY4R* duplicon as observed in H10 haplotype (**Fig. 4B**). We restricted H11 breakpoint to a 1,641 bp interval that corresponds to intron 26 of *FRMPD2/2B* genes (**Fig. 4A**, **Table 3**, **Supplemental Fig. S6, Supplemental Table S3**) and H10 breakpoint to a ~20 kbp interval overlapping *FAM245B* (**Fig. 4B**, **Table 3**, **Supplemental Fig. S7, Supplemental Table S3**).

Finally, we evaluated features that have been previously associated with breakpoint sequences of NAHR events, i.e. long stretches of homology between non-allelic sequences, high GC content, and presence of PRDM9 binding motifs. We assessed both the length and homology of SDs mediating the rearrangements, as well as those of the refined breakpoint intervals. In the latter, we also checked GC content and presence of PRDM9 motifs (**Table 3**). While the length and homology of the entire SD pairs are variable, with the H3 rearrangement mediated by a pair with low similarity, diversity plots indicate that NAHR crossing overs tend to occur at positions with higher identity between parental SDs (99.64–100%), as shown by reference lines (**Fig. 3B, C, Table 3, Supplemental Fig. S2, S3, S5, S6, S7**). We also observe a GC content higher than the human genome average of 40.9% (Piovesan et al. 2019) at 7 out of 10 breakpoints (**Table 3**), while we identified no enrichment in PRDM9 motifs when we compared breakpoint intervals *versus* the rest of the SD sequences (Fisher's exact test, $P = 1$).

Phylogenetic analysis of *AGAP* duplicons

Breakpoint sequence analysis revealed that alternative haplotypes derive from NAHR between SD pairs located in clusters that share the occurrence of a functional or pseudogenized *AGAP* copy (**Fig. 1A**). Among the 13 *AGAP* copies annotated in the human reference genome, *AGAP1*, *AGAP2*, and *AGAP3* have 1:1 orthologs in vertebrate genomes, including marmoset and mouse lemur (**Table 1**, GENCODE v44 and Ensembl release 110). The remaining ten copies map on Chromosome 10, with the majority (7/10) at the q-arm pericentromeric region, precisely 10q11.22 (**Table 1**). They consist in four protein-coding genes, five pseudogenes, and one noncoding RNA gene. These ten copies correspond to a ~22 kbp genomic segment, except *AGAP11* that is shorter and corresponds to a ~9 kbp segment. Except *AGAP9* that has a 1:1 ortholog in *Gorilla gorilla*, these ten copies do not have 1:1 orthologs in other genomes. Conversely, they have 1:many or many:many orthologs in species belonging to the Catarrhini parvorder of Primates that includes Old World monkeys and apes.

We analyzed the organization, synteny relationships, and phylogeny of human *AGAP* copies located on Chromosome 10 in comparison with other great apes. Through BLAT search using human *AGAP4* genomic sequence as query, we identified the location of Chromosome 10 *AGAP* genes in the chimpanzee (panTro6), gorilla (gorGor6), and orangutan (ponAbe3) genomes. In chimpanzee, we identified *AGAP* sequences at five locations on Chromosome 10, as well as complete or partial alignments in four unlocalized contigs (chrUn). In gorilla, three *AGAP* sequences are located on Chromosome 10, with two additional partial matches in unlocalized contigs that probably correspond to one copy. In orangutan, we identified partial alignments at five locations in a 5 Mbp gap-rich 10q11 pericentromeric interval as well as additional shorter matches in unlocalized contigs. These data show that a cluster of *AGAP* copies is present at the pericentromeric region of the long arm of Chromosome 10 in human, chimpanzee, and orangutan and it likely reflects the ancestral ape organization of this catarrhine-specific subgroup of the *AGAP* family (**Fig. 5A**). Although genome references report a higher number of copies in humans and chimpanzees compared to other apes, *AGAP* copy-number estimates suggest an expansion in gorillas similar to that in chimpanzees (**Fig. 2A**).

Pairwise genomic sequence alignments of human versus other primates (UCSC track of net alignments) revealed numerous breaks of synteny between genomes and complex rearrangements at this locus (**Fig. 5B**). This feature, together with the presence of several *AGAP* sequences in unlocalized contigs of ape genome assemblies, hampered the identification of 1:1 orthology relationships between the majority of Chromosome 10 *AGAP* copies. An evolutionary pericentric inversion in the African ape ancestor moved one *AGAP* copy (*AGAP11*) more distally and outside the pericentromeric cluster. This is the only copy for which the orthology relationship between human, chimpanzee, and gorilla genes is straightforward.

Next, we built a phylogeny based on a 5 kbp segment that is shared among all human *AGAP* copies. We retrieved *AGAP* genomic sequences for human (n = 10), chimpanzee (n = 8), gorilla (n = 4), and orangutan (n = 2). As the presence of gaps in the orangutan genome assembly might limit the recovery of sequences corresponding to our query, we searched for fully sequenced *Pongo abelii* BAC clones containing *AGAP* sequences. We identified two clones (CH276-56H17 and CH276-327M15) that embedded one missing sequence. We noted that these clones correspond to the proximal African ape inversion breakpoint and *AGAP* and *FAM25* sequences are located within the 26 kbp breakpoint interval. The phylogeny reveals a monophyletic clade that includes human, chimp, and gorilla *AGAP11* copies. Conversely, all other *AGAP* genes cluster by species, probably because of gene conversion among closely located *AGAP* members (**Fig. 5C**). Human pericentromeric *AGAP* copies cluster in two main clades both supported by high bootstrap values. One clade includes *AGAP4*, *AGAP6*, *AGAP7P*, *AGAP10P*, and *AGAP13P*, while the other comprises *AGAP5*, *AGAP9*, *AGAP12P*, and *AGAP14P*. *AGAP* copies at 10q11.22 SD clusters belong to both groups. By applying the molecular clock approach and calibrating the tree based on a human/chimpanzee divergence time of 6.4 million years ago, we estimated that split events between human pericentromeric *AGAP* copies happened between 5.7 and 1.4 million years ago (**Fig. 5C**).

Discussion

In this work, we took advantage of recent advancements in research resources, that is, the release of the first gapless human genome (Nurk et al. 2022) and the *de novo* assembly of diverse human genomes (Chaisson et al. 2019; Liao et al. 2023), to study the genomic organization and structural variation of human Chromosome 10q11.22. Our sequence analysis revealed extensive structural diversity, including large-scale (> 50 kbp) deletions, duplications, and inversions that originate from SD-mediated NAHR. We identified 11 alternative structures, each differing in size from the most common haplotype (H1) by as much as 20 kbp up to 1.7 Mbp. We believe that this catalogue does not encompass the full spectrum of structural variation at this locus. For instance, eight structures were unique to a single genome, indicating that analyzing additional genomes might reveal novel arrangements. We note that according to our WSSD and SUNK copy-number estimates, some individuals carry more than four *PTPN20* copies, yet all haplotypes that we describe have one or two copies. It is possible that some individuals carry the reciprocal product (duplication) of the NAHR generating the H11 deletion haplotype and therefore carry five *PTPN20* diploid copies. This region was unassembled in about one-third of the genomes in the initial set (30 out of 94). As copy-number data for these samples, when available, align with an H1-H1 genotype, the lack of successful assembly could be due to the presence of highly repetitive DNA, such as long stretches of simple repeats, or structural mosaicism within the same cell line. However, neither possibility would impact the conclusions of the present study.

SUNK estimates of paralogous genes within copy-number variant segments do not always align with expectations. We believe that some discrepancies result from inversion toggling mediated by *NPY4R* inverted duplicons (Porubsky et al. 2020; Porubsky et al. 2022), which mixes paralogous copies of genes located on these segments. Additionally, gene conversion events might also contribute to the observed differences. Human *AGAP* WSSD estimates typically range around 19 or 20 in H1-H1 samples, with 20 being the expected value. This discrepancy is likely due to limitations in WSSD genotyping, particularly for high-copy-number genes.

Breakpoint analysis in five genomes with the same inversion showed they derive from different NAHR events mediated by the same SD pair but with breakpoints at diverse positions. We noticed intervals within some of the derived SD hybrid sequences where the similarity to the parental SD copies is not as anticipated. These patterns might derive from either subsequent gene conversion with the SD copy on the homologous chromosome or additional inversion events (inversion toggling) and subsequent recombination in the region between the inverted SDs. Indeed, there is evidence of mutational toggling for this inversion (Porubsky et al. 2020; Porubsky et al. 2022) and of recombination in the *GDF10* segment (**Supplemental Fig. 1**).

Previous studies have demonstrated that several factors influence the likelihood of NAHR, including the length, homology, and distance between non-allelic duplicate sequences, as well as the GC content, presence of tracts of perfect sequence identity, PRDM9 binding sites, G-quadruplex forming sequences, and local recombination activity (Lupski 1998; Lindsay et al. 2006; Liu et al. 2011; Dittwald et al. 2013; Hillmer et al. 2016; Summerer et al. 2018). In this study, we analyzed the occurrence of some of these features in ten finely mapped breakpoint sequences and found that the presence of tracts of perfect or almost perfect sequence identity is a selective requirement of NAHR crossing over sites, regardless of the overall similarity of the SD pair. The presence of PRDM9 binding sites, G-quadruplex forming sequences, and local recombination activity could not be assessed due to missing data on SD regions in genome-wide studies that evaluated these features (Altemose et al. 2017; Hansel-Hertsch et al. 2018).

The 10q11.22 SD architecture and rearrangement breakpoints are associated with a catarrhine-specific subgroup of the *AGAP* gene family that likely triggered the accumulation of SDs at this locus in the last 25 million years of human evolution. The *AGAP* family includes *AGAP1*, *AGAP2*, and *AGAP3* that have 1:1 orthologs in vertebrate genomes, as well as *AGAP4* to *AGAP14* that map on Chromosome 10 and are more recent genes. These additional copies began to emerge in the common ancestor of apes and Old World monkeys by duplication at the pericentromeric region of ancestral Chromosome 10. Evolutionary genomic rearrangements, assembly gaps in ape genome references, and interlocus gene conversion hamper the identification of ancestral Chromosome 10 copies, 1:1 orthology relationships between ape genomes, and lineage-specific more recent copies. The incompleteness of *AGAP* sequences in ape reference genomes is reflected by numerous matches in unlocalized contigs and by the discrepancy between the number of copies annotated in the genomes and the number of WSSD-predicted copies, especially in gorillas.

AGAP proteins, previously referred to as members of the gamma subgroup of the centaurin superfamily of small GTPases (centaurin gamma), are characterized by a pleckstrin homology (PH) domain, an Arf GTPase activating (ArfGAP) domain, and ankyrin repeats (Kahn et al. 2008). AGAP1 and AGAP2 have been the most studied members and have roles in endosomal trafficking and cytoskeleton dynamics (Nie et al. 2002; Nie et al. 2005). In particular, AGAP1 was shown to control cytoskeleton remodeling involved in cell movement (Luo et al. 2016), while AGAP2 was shown to regulate retrograde transport between early endosomes and the trans-Golgi network (Shiba et al. 2010) and to modulate the disassembly of focal adhesions during cell migration (Zhu et al. 2009). AGAP proteins have specialized functions in neurons. AGAP1 was shown to participate in dendritic spine morphology (Arnold et al. 2016) and endocytic recycling of muscarinic receptors (Bendor et al. 2010). AGAP2 has several roles in the central nervous system, including neurite outgrowth (Dwane et al. 2014), myelination (Chan et al. 2014), regulation of glutamate receptors at synapses (Chan et al. 2011a), neuronal survival (Tang et al. 2008), and memory formation (Chan et al. 2011b). AGAP3 was proposed to have a role in contextual novelty-induced memory consolidation by regulating glutamate receptor trafficking in the synapse (Oku and Huganir 2013; Hojgaard et al. 2023). To our knowledge, functional studies on the primate-specific *AGAP* genes have not been reported in the literature. It is possible that primate-specific functional *AGAP* copies have similar roles at neuronal synapses. This suggests that *AGAP* expansion might have enhanced synaptic plasticity and advanced memory functions in primates and humans.

The promotion of further duplicative transposition events and the creation of complex SD clusters around *AGAP* duplicons recall the behavior of other elements in human and primate genomes, like *LRRC37* copies on Chromosome 17 (Giannuzzi et al. 2013b), *GOLGA* copies on Chromosome 15 (Giannuzzi et al. 2013a; Antonacci et al. 2014; Maggiolini et al. 2019), and *NPIP* copies on Chromosome 16 (Nuttle et al. 2016; Cantsilieris et al. 2020). *LRRC37*, *GOLGA*, and *NPIP* are all classified as core duplicons (Jiang et al. 2007).

The extensive diversity at Chromosome 10q11.22 reminds that of other regions like 3q29 (Yilmaz et al. 2023), 22q11 (Demaerel et al. 2019), 17q21.31 (Steinberg et al. 2012), and

16p11.2 (Nuttle et al. 2016; Loviglio et al. 2017; Giannuzzi et al. 2019; Giannuzzi et al. 2022), where copy-number variant segments and inversion polymorphisms give rise to multiple structural haplotypes differing in up to a few millions of base pairs. Additionally, this locus provides another example of how large inversion polymorphisms may alter the whole SD arrangement, generating new predispositions to copy-number variations. In fact, a similar pattern occurs at the 17q21.31 Koolen de Vries syndrome region (Koolen et al. 2006) and 7q11 Williams-Beuren syndrome region (Osborne et al. 2001).

Our detailed map of polymorphic structural variants will aid in identifying potential pathogenic structures at this locus. The pathogenicity and association of 10q11 deletions and duplications involving *GPRIN2* and other genes with neurodevelopmental and neuropsychiatric diseases remain unclear, possibly due to the structural complexity and diversity of the locus, as well as the potential low penetrance and variable expressivity of the variants (Cooper et al. 2011; Stankiewicz et al. 2012; Coe et al. 2014).

Methods

Structural variation analysis

We downloaded diploid assemblies of 47 samples (94 haplotypes) from https://github.com/human-pangenomics/HPP_Year1_Assemblies (Liao et al. 2023). We obtained Chr10:44,500,000-50,500,000 sequence from the T2T-CHM13 genome (v2.0) and aligned it to each genome using minimap2 v2.24 (Li 2018). We kept for further analysis the haplotypes where the 10q11.22 region was fully assembled (i.e., present in a single contig). We compared the sequences with the reference T2T-CHM13 sequence using the re-DOT-able tool (https://www.bioinformatics.babraham.ac.uk/projects/redotable/). We verified the assemblies using GAVISUNK (Dishuck et al. 2023). Figure 1B was created in R (R Core

Team 2023) using the ggplot2 v3.4.4 (Wickham 2009) and gggenomes (Hackl et al. 2023) packages.

Copy numbers were estimated using the WSSD (Bailey et al. 2002) and SUNK (Sudmant et al. 2010) methods. The WSSD method estimates total copy number for sequence ≥95% sequence identity in non-overlapping 1 kbp genomic windows based on the depth of coverage of whole-genome Illumina short reads aligned to the reference genome. The SUNK-based method estimates the paralog-specific copy number. Correlations were calculated using the Spearman's method and the correlation matrix between copy-number estimates was obtained using the scales v1.2.1 (Wickham and Seidel 2022) and ggcorrplot v0.1.4.1 (Kassambara 2023) R packages.

Breakpoint analysis

We identified approximate breakpoint regions by aligning each haplotype sequence to the H1 sequence using BLAST (Basic Local Alignment Search Tool) (Altschul et al. 1990). We mapped the approximate breakpoint region in the T2T-CHM13 v2.0 genome by BLAT (Kent 2002) and pinpointed the SD pair that putatively mediated the NAHR event originating the new haplotype. We multialigned the original SD sequences from T2T genome and the sequence of the "chimeric" SD sequence/s at the breakpoint from the variant haplotype using MAFFT (Katoh et al. 2009). We calculated pairwise nucleotide diversity in 500 bp sliding windows with a 100 bp increment by using the PopGenome R package (Pfeifer et al. 2014) and narrowed down the location of the breakpoint by visual inspection of the resulting plots and the multialignment. We refined the breakpoint at the position where the breakpoint sequence becomes more similar from one duplication to the other of the pair.

We assessed annotation of genes (CAT + Liftoff Gene Annotations UCSC track), repetitive elements content (RepeatMasker Repetitive Elements UCSC track), and GC content (GC Percent in 5-Base Windows UCSC track) of breakpoint sequences. We analyzed the presence of PRDM9 motif (5′ CCNCCNTNNCCNC 3′) by using the FIMO MEME-suite (Grant et al. 2011).

Evolutionary analyses

We multialigned human *AGAP* genomic sequences using MAFFT and calculated pairwise divergences. We located *AGAP* sequences in ape genomes through BLAT search and visual inspection of the resulting alignments. To reconstruct *AGAP* phylogeny, we used a 5 kbp sequence nearly corresponding to exon 6 – intron 6 – exon 7 – intron 7 – exon 8 of *AGAP4* genomic sequence (gene structure based on MANE transcript annotation). We retrieved human and ape *AGAP* sequences through BLAT search in human (hg38), chimpanzee (panTro6), gorilla (gorGor6), and orangutan (ponAbe3) genomes. Sequences were multialigned by ClustalW (Thompson et al. 1994). The phylogeny was inferred by using the Maximum Likelihood method and Kimura 2-parameter model (Kimura 1980). All positions containing gaps and missing data were eliminated (complete deletion option). Statistical significance of nodes was evaluated by using the bootstrap test with 100 replicates (Felsenstein 1985). To date the expansion of *AGAP* copies in humans, we built a phylogenetic tree of human *AGAP* pericentromeric copies (i.e., excluding *AGAP11*) with one chimpanzee (Ptr_42) and one orangutan (Pab_45) sequence. After testing the molecular clock hypothesis using the Maximum Likelihood method, we inferred evolutionary timing of human duplications. We used the orangutan sequence as the outgroup and calibrated the tree by assigning a fixed time of human-chimpanzee split at 6.4 million years ago. Evolutionary analyses were conducted in MEGAX (Kumar et al. 2018; Stecher et al. 2020).

Competing interest statement

E.E.E. is a scientific advisory board (SAB) member of Variant Bio, Inc.

Acknowledgments

This study received funding from the European Union – Next Generation EU - National Recovery and Resilience Plan (NRRP), Mission 4, Component 2, Investment 1.1, call PRIN 2022 D.D. 104 02.02.2022 to G.G. (2022RB88C7). This work was supported, in part, by US National Institutes of Health (NIH) grant HG002385 to E.E.E. We thank Paolo Carnevali and Sara Simmonds for providing access to data. We thank Paolo Gandellini for discussions and Tonia Brown for assistance in manuscript editing. E.E.E. is an investigator of the Howard Hughes Medical Institute.

Author contributions: G.G. conceived and supervised the study. S.F., V.S.D., and G.G. analyzed pangenome data. P.C.D. performed the GAVISUNK analysis. S.F. performed the breakpoint analysis. W.T.H. and E.E.E. provided copy-number estimates. S.F. and G.G. analyzed copy-number estimates. V.S.D. and G.G. performed evolutionary analysis of *AGAP* genes. G.G. wrote the manuscript. All authors read and approved the manuscript.

References

Aerts E, Beckers S, Zegers D, Van Hoorenbeeck K, Massa G, Verrijken A, Verhulst SL, Van Gaal LF, Van Hul W. 2016. CNV analysis and mutation screening indicate an important role for the NPY4R gene in human obesity. *Obesity (Silver Spring)* **24**: 970-976.

Altemose N, Noor N, Bitoun E, Tumian A, Imbeault M, Chapman JR, Aricescu AR, Myers SR. 2017. A map of human PRDM9 binding provides evidence for novel behaviors of PRDM9 and other zinc-finger proteins in meiosis. *Elife* **6**.

Altschul SF, Gish W, Miller W, Myers EW, Lipman DJ. 1990. Basic local alignment search tool. *J Mol Biol* **215**: 403-410.

Antonacci F, Dennis MY, Huddleston J, Sudmant PH, Steinberg KM, Rosenfeld JA, Miroballo M, Graves TA, Vives L, Malig M et al. 2014. Palindromic GOLGA8 core duplicons promote chromosome 15q13.3 microdeletion and evolutionary instability. *Nat Genet* **46**: 1293-1302.

Arnold M, Cross R, Singleton KS, Zlatic S, Chapleau C, Mullin AP, Rolle I, Moore CC, Theibert A, Pozzo-Miller L et al. 2016. The Endosome Localized Arf-GAP AGAP1 Modulates Dendritic Spine Morphology Downstream of the Neurodevelopmental Disorder Factor Dysbindin. *Front Cell Neurosci* **10**: 218.

Bailey JA, Eichler EE. 2006. Primate segmental duplications: crucibles of evolution, diversity and disease. *Nat Rev Genet* **7**: 552-564.

Bailey JA, Gu Z, Clark RA, Reinert K, Samonte RV, Schwartz S, Adams MD, Myers EW, Li PW, Eichler EE. 2002. Recent segmental duplications in the human genome. *Science* **297**: 1003-1007.

Bailey JA, Yavor AM, Massa HF, Trask BJ, Eichler EE. 2001. Segmental duplications: organization and impact within the current human genome project assembly. *Genome Res* **11**: 1005-1017.

Bendor J, Lizardi-Ortiz JE, Westphalen RI, Brandstetter M, Hemmings HC, Jr., Sulzer D, Flajolet M, Greengard P. 2010. AGAP1/AP-3-dependent endocytic recycling of M5 muscarinic receptors promotes dopamine release. *EMBO J* **29**: 2813-2826.

Cantsilieris S, Sunkin SM, Johnson ME, Anaclerio F, Huddleston J, Baker C, Dougherty ML, Underwood JG, Sulovari A, Hsieh P et al. 2020. An evolutionary driver of interspersed segmental duplications in primates. *Genome Biol* **21**: 202.

Carvalho CM, Lupski JR. 2016. Mechanisms underlying structural variant formation in genomic disorders. *Nat Rev Genet* **17**: 224-238.

Chaisson MJ, Huddleston J, Dennis MY, Sudmant PH, Malig M, Hormozdiari F, Antonacci F, Surti U, Sandstrom R, Boitano M et al. 2015. Resolving the complexity of the human genome using single-molecule sequencing. *Nature* **517**: 608-611.

Chaisson MJP, Sanders AD, Zhao X, Malhotra A, Porubsky D, Rausch T, Gardner EJ, Rodriguez OL, Guo L, Collins RL et al. 2019. Multi-platform discovery of haplotype-resolved structural variation in human genomes. *Nat Commun* **10**: 1784.

Chan CB, Chen Y, Liu X, Tang X, Lee CW, Mei L, Ye K. 2011a. PIKE-mediated PI3-kinase activity is required for AMPA receptor surface expression. *EMBO J* **30**: 4274-4286.

Chan CB, Liu X, Pradoldej S, Hao C, An J, Yepes M, Luo HR, Ye K. 2011b. Phosphoinositide 3-kinase enhancer regulates neuronal dendritogenesis and survival in neocortex. *J Neurosci* **31**: 8083-8092.

Chan CB, Liu X, Zhao L, Liu G, Lee CW, Feng Y, Ye K. 2014. PIKE is essential for oligodendroglia development and CNS myelination. *Proc Natl Acad Sci U S A* **111**: 1993-1998.

Chen J, Calhoun VD, Perrone-Bizzozero NI, Pearlson GD, Sui J, Du Y, Liu J. 2016. A pilot study on commonality and specificity of copy number variants in schizophrenia and bipolar disorder. *Transl Psychiatry* **6**: e824.

Cheng H, Concepcion GT, Feng X, Zhang H, Li H. 2021. Haplotype-resolved de novo assembly using phased assembly graphs with hifiasm. *Nat Methods* **18**: 170-175.

Coe BP, Witherspoon K, Rosenfeld JA, van Bon BW, Vulto-van Silfhout AT, Bosco P, Friend KL, Baker C, Buono S, Vissers LE et al. 2014. Refining analyses of copy number variation identifies specific genes associated with developmental delay. *Nat Genet* **46**: 1063-1071.

Cooper GM, Coe BP, Girirajan S, Rosenfeld JA, Vu TH, Baker C, Williams C, Stalker H, Hamid R, Hannig V et al. 2011. A copy number variation morbidity map of developmental delay. *Nat Genet* **43**: 838-846.

Demaerel W, Mostovoy Y, Yilmaz F, Vervoort L, Pastor S, Hestand MS, Swillen A, Vergaelen E, Geiger EA, Coughlin CR et al. 2019. The 22q11 low copy repeats are characterized by unprecedented size and structural variability. *Genome Res* **29**: 1389-1401.

Dennis MY, Harshman L, Nelson BJ, Penn O, Cantsilieris S, Huddleston J, Antonacci F, Penewit K, Denman L, Raja A et al. 2017. The evolution and population diversity of human-specific segmental duplications. *Nat Ecol Evol* **1**: 69.

Dishuck PC, Rozanski AN, Logsdon GA, Porubsky D, Eichler EE. 2023. GAVISUNK: genome assembly validation via inter-SUNK distances in Oxford Nanopore reads. *Bioinformatics* **39**.

Dittwald P, Gambin T, Szafranski P, Li J, Amato S, Divon MY, Rodriguez Rojas LX, Elton LE, Scott DA, Schaaf CP et al. 2013. NAHR-mediated copy-number variants in a clinical population: mechanistic insights into both genomic disorders and Mendelizing traits. *Genome Res* **23**: 1395-1409.

Dwane S, Durack E, O'Connor R, Kiely PA. 2014. RACK1 promotes neurite outgrowth by scaffolding AGAP2 to FAK. *Cell Signal* **26**: 9-18.

Felsenstein J. 1985. Confidence Limits on Phylogenies: An Approach Using the Bootstrap. *Evolution* **39**: 783-791.

Giannuzzi G, Chatron N, Mannik K, Auwerx C, Pradervand S, Willemin G, Hoekzema K, Nuttle X, Chrast J, Sadler MC et al. 2022. Possible association of 16p11.2 copy number variation with altered lymphocyte and neutrophil counts. *NPJ Genom Med* **7**: 38.

Giannuzzi G, Migliavacca E, Reymond A. 2014. Novel H3K4me3 marks are enriched at human- and chimpanzee-specific cytogenetic structures. *Genome Res* **24**: 1455-1468.

Giannuzzi G, Pazienza M, Huddleston J, Antonacci F, Malig M, Vives L, Eichler EE, Ventura M. 2013a. Hominoid fission of chromosome 14/15 and the role of segmental duplications. *Genome Res* **23**: 1763-1773.

Giannuzzi G, Schmidt PJ, Porcu E, Willemin G, Munson KM, Nuttle X, Earl R, Chrast J, Hoekzema K, Risso D et al. 2019. The Human-Specific BOLA2 Duplication Modifies Iron Homeostasis and Anemia Predisposition in Chromosome 16p11.2 Autism Individuals. *Am J Hum Genet* **105**: 947-958.

Giannuzzi G, Siswara P, Malig M, Marques-Bonet T, Program NCS, Mullikin JC, Ventura M, Eichler EE. 2013b. Evolutionary dynamism of the primate LRRC37 gene family. *Genome Res* **23**: 46-59.

Grant CE, Bailey TL, Noble WS. 2011. FIMO: scanning for occurrences of a given motif. *Bioinformatics* **27**: 1017-1018.

Hackl T, Ankenbrand MJ, van Adrichem B. 2023. gggenomes: A Grammar of Graphics for Comparative Genomics.

Handsaker RE, Van Doren V, Berman JR, Genovese G, Kashin S, Boettger LM, McCarroll SA. 2015. Large multiallelic copy number variations in humans. *Nat Genet* **47**: 296-303.

Hansel-Hertsch R, Spiegel J, Marsico G, Tannahill D, Balasubramanian S. 2018. Genome-wide mapping of endogenous G-quadruplex DNA structures by chromatin immunoprecipitation and high-throughput sequencing. *Nat Protoc* **13**: 551-564.

Hillmer M, Wagner D, Summerer A, Daiber M, Mautner VF, Messiaen L, Cooper DN, Kehrer-Sawatzki H. 2016. Fine mapping of meiotic NAHR-associated crossovers causing large NF1 deletions. *Hum Mol Genet* **25**: 484-496.

Hojgaard K, Szollosi B, Henningsen K, Minami N, Nakanishi N, Kaadt E, Tamura M, Morris RGM, Takeuchi T, Elfving B. 2023. Novelty-induced memory consolidation is accompanied by increased Agap3 transcription: a cross-species study. *Mol Brain* **16**: 69.

Jarick I, Vogel CI, Scherag S, Schafer H, Hebebrand J, Hinney A, Scherag A. 2011. Novel common copy number variation for early onset extreme obesity on chromosome 11q11 identified by a genome-wide analysis. *Hum Mol Genet* **20**: 840-852.

Jiang Z, Tang H, Ventura M, Cardone MF, Marques-Bonet T, She X, Pevzner PA, Eichler EE. 2007. Ancestral reconstruction of segmental duplications reveals punctuated cores of human genome evolution. *Nat Genet* **39**: 1361-1368.

Kahn RA, Bruford E, Inoue H, Logsdon JM, Jr., Nie Z, Premont RT, Randazzo PA, Satake M, Theibert AB, Zapp ML et al. 2008. Consensus nomenclature for the human ArfGAP domain-containing proteins. *J Cell Biol* **182**: 1039-1044.

Kassambara A. 2023. ggcorrplot: Visualization of a Correlation Matrix using 'ggplot2'.

Katoh K, Asimenos G, Toh H. 2009. Multiple alignment of DNA sequences with MAFFT. *Methods Mol Biol* **537**: 39-64.

Kent WJ. 2002. BLAT--the BLAST-like alignment tool. *Genome Res* **12**: 656-664.

Kimura M. 1980. A simple method for estimating evolutionary rates of base substitutions through comparative studies of nucleotide sequences. *J Mol Evol* **16**: 111-120.

Koolen DA, Vissers LE, Pfundt R, de Leeuw N, Knight SJ, Regan R, Kooy RF, Reyniers E, Romano C, Fichera M et al. 2006. A new chromosome 17q21.31 microdeletion syndrome associated with a common inversion polymorphism. *Nat Genet* **38**: 999-1001.

Kumar S, Stecher G, Li M, Knyaz C, Tamura K. 2018. MEGA X: Molecular Evolutionary Genetics Analysis across Computing Platforms. *Mol Biol Evol* **35**: 1547-1549.

Li H. 2018. Minimap2: pairwise alignment for nucleotide sequences. *Bioinformatics* **34**: 3094-3100.

Liao WW Asri M Ebler J Doerr D Haukness M Hickey G Lu S Lucas JK Monlong J Abel HJ et al. 2023. A draft human pangenome reference. *Nature* **617**: 312-324.

Lindsay SJ, Khajavi M, Lupski JR, Hurles ME. 2006. A chromosomal rearrangement hotspot can be identified from population genetic variation and is coincident with a hotspot for allelic recombination. *Am J Hum Genet* **79**: 890-902.

Liu P, Lacaria M, Zhang F, Withers M, Hastings PJ, Lupski JR. 2011. Frequency of nonallelic homologous recombination is correlated with length of homology: evidence that ectopic synapsis precedes ectopic crossing-over. *Am J Hum Genet* **89**: 580-588.

Loviglio MN, Arbogast T, Jonch AE, Collins SC, Popadin K, Bonnet CS, Giannuzzi G, Maillard AM, Jacquemont S, p C et al. 2017. The Immune Signaling Adaptor LAT Contributes to the Neuroanatomical Phenotype of 16p11.2 BP2-BP3 CNVs. *Am J Hum Genet* **101**: 564-577.

Luo R, Chen PW, Wagenbach M, Jian X, Jenkins L, Wordeman L, Randazzo PA. 2016. Direct functional interaction of the kinesin-13 family member kinesin-like protein 2A (Kif2A) and Arf GAP with GTP-binding protein-like, ankyrin repeats and PH domains 1 (AGAP1). *J Biol Chem* **291**: 25761.

Lupski JR. 1998. Genomic disorders: structural features of the genome can lead to DNA rearrangements and human disease traits. *Trends Genet* **14**: 417-422.

Maggiolini FAM, Cantsilieris S, D'Addabbo P, Manganelli M, Coe BP, Dumont BL, Sanders AD, Pang AWC, Vollger MR, Palumbo O et al. 2019. Genomic inversions and GOLGA core duplicons underlie disease instability at the 15q25 locus. *PLoS Genet* **15**: e1008075.

Marques-Bonet T, Kidd JM, Ventura M, Graves TA, Cheng Z, Hillier LW, Jiang Z, Baker C, Malfavon-Borja R, Fulton LA et al. 2009. A burst of segmental duplications in the genome of the African great ape ancestor. *Nature* **457**: 877-881.

Migliavacca E, Golzio C, Mannik K, Blumenthal I, Oh EC, Harewood L, Kosmicki JA, Loviglio MN, Giannuzzi G, Hippolyte L et al. 2015. A Potential Contributory Role for Ciliary Dysfunction in the 16p11.2 600 kb BP4-BP5 Pathology. *Am J Hum Genet* **96**: 784-796.

Nie Z, Fei J, Premont RT, Randazzo PA. 2005. The Arf GAPs AGAP1 and AGAP2 distinguish between the adaptor protein complexes AP-1 and AP-3. *J Cell Sci* **118**: 3555-3566.

Nie Z, Stanley KT, Stauffer S, Jacques KM, Hirsch DS, Takei J, Randazzo PA. 2002. AGAP1, an endosome-associated, phosphoinositide-dependent ADP-ribosylation factor GTPase-activating protein that affects actin cytoskeleton. *J Biol Chem* **277**: 48965-48975.

Numanagic I, Gokkaya AS, Zhang L, Berger B, Alkan C, Hach F. 2018. Fast characterization of segmental duplications in genome assemblies. *Bioinformatics* **34**: i706-i714.

Nurk S, Koren S, Rhie A, Rautiainen M, Bzikadze AV, Mikheenko A, Vollger MR, Altemose N, Uralsky L, Gershman A et al. 2022. The complete sequence of a human genome. *Science* **376**: 44-53.

Nuttle X, Giannuzzi G, Duyzend MH, Schraiber JG, Narvaiza I, Sudmant PH, Penn O, Chiatante G, Malig M, Huddleston J et al. 2016. Emergence of a Homo sapiens-specific gene family and chromosome 16p11.2 CNV susceptibility. *Nature* **536**: 205-209.

Oku Y, Huganir RL. 2013. AGAP3 and Arf6 regulate trafficking of AMPA receptors and synaptic plasticity. *J Neurosci* **33**: 12586-12598.

Osborne LR, Li M, Pober B, Chitayat D, Bodurtha J, Mandel A, Costa T, Grebe T, Cox S, Tsui LC et al. 2001. A 1.5 million-base pair inversion polymorphism in families with Williams-Beuren syndrome. *Nat Genet* **29**: 321-325.

Pfeifer B, Wittelsburger U, Ramos-Onsins SE, Lercher MJ. 2014. PopGenome: an efficient Swiss army knife for population genomic analyses in R. *Mol Biol Evol* **31**: 1929-1936.

Piovesan A, Pelleri MC, Antonaros F, Strippoli P, Caracausi M, Vitale L. 2019. On the length, weight and GC content of the human genome. *BMC Res Notes* **12**: 106.

Porubsky D, Hops W, Ashraf H, Hsieh P, Rodriguez-Martin B, Yilmaz F, Ebler J, Hallast P, Maria Maggiolini FA, Harvey WT et al. 2022. Recurrent inversion polymorphisms in humans associate with genetic instability and genomic disorders. *Cell* **185**: 1986-2005 e1926.

Porubsky D, Sanders AD, Hops W, Hsieh P, Sulovari A, Li R, Mercuri L, Sorensen M, Murali SC, Gordon D et al. 2020. Recurrent inversion toggling and great ape genome evolution. *Nat Genet* **52**: 849-858.

Priebe L, Degenhardt FA, Herms S, Haenisch B, Mattheisen M, Nieratschker V, Weingarten M, Witt S, Breuer R, Paul T et al. 2012. Genome-wide survey implicates the influence of copy number variants (CNVs) in the development of early-onset bipolar disorder. *Mol Psychiatry* **17**: 421-432.

R Core Team. 2023. R: A language and environment for statistical computing., https://www.R-project.org/.

Sha BY, Yang TL, Zhao LJ, Chen XD, Guo Y, Chen Y, Pan F, Zhang ZX, Dong SS, Xu XH et al. 2009. Genome-wide association study suggested copy number variation may be associated with body mass index in the Chinese population. *J Hum Genet* **54**: 199-202.

Shafin K, Pesout T, Lorig-Roach R, Haukness M, Olsen HE, Bosworth C, Armstrong J, Tigyi K, Maurer N, Koren S et al. 2020. Nanopore sequencing and the Shasta toolkit enable efficient de novo assembly of eleven human genomes. *Nat Biotechnol* **38**: 1044-1053.

Shebanits K, Andersson-Assarsson JC, Larsson I, Carlsson LMS, Feuk L, Larhammar D. 2018. Copy number of pancreatic polypeptide receptor gene NPY4R correlates with body mass index and waist circumference. *PLoS One* **13**: e0194668.

Shiba Y, Romer W, Mardones GA, Burgos PV, Lamaze C, Johannes L. 2010. AGAP2 regulates retrograde transport between early endosomes and the TGN. *J Cell Sci* **123**: 2381-2390.

Stankiewicz P, Kulkarni S, Dharmadhikari AV, Sampath S, Bhatt SS, Shaikh TH, Xia Z, Pursley AN, Cooper ML, Shinawi M et al. 2012. Recurrent deletions and reciprocal duplications of 10q11.21q11.23 including CHAT and SLC18A3 are likely mediated by complex low-copy repeats. *Hum Mutat* **33**: 165-179.

Stankiewicz P, Lupski JR. 2002. Genome architecture, rearrangements and genomic disorders. *Trends Genet* **18**: 74-82.

Stecher G, Tamura K, Kumar S. 2020. Molecular Evolutionary Genetics Analysis (MEGA) for macOS. *Mol Biol Evol* **37**: 1237-1239.

Steinberg KM, Antonacci F, Sudmant PH, Kidd JM, Campbell CD, Vives L, Malig M, Scheinfeldt L, Beggs W, Ibrahim M et al. 2012. Structural diversity and African origin of the 17q21.31 inversion polymorphism. *Nat Genet* **44**: 872-880.

Sudmant PH, Kitzman JO, Antonacci F, Alkan C, Malig M, Tsalenko A, Sampas N, Bruhn L, Shendure J, Genomes P et al. 2010. Diversity of human copy number variation and multicopy genes. *Science* **330**: 641-646.

Summerer A, Mautner VF, Upadhyaya M, Claes KBM, Hogel J, Cooper DN, Messiaen L, Kehrer-Sawatzki H. 2018. Extreme clustering of type-1 NF1 deletion breakpoints co-locating with G-quadruplex forming sequences. *Hum Genet* **137**: 511-520.

Tang X, Jang SW, Okada M, Chan CB, Feng Y, Liu Y, Luo SW, Hong Y, Rama N, Xiong WC et al. 2008. Netrin-1 mediates neuronal survival through PIKE-L interaction with the dependence receptor UNC5B. *Nat Cell Biol* **10**: 698-706.

Thompson JD, Higgins DG, Gibson TJ. 1994. CLUSTAL W: improving the sensitivity of progressive multiple sequence alignment through sequence weighting, position-specific gap penalties and weight matrix choice. *Nucleic Acids Res* **22**: 4673-4680.

Vollger MR, Dishuck PC, Sorensen M, Welch AE, Dang V, Dougherty ML, Graves-Lindsay TA, Wilson RK, Chaisson MJP, Eichler EE. 2019. Long-read sequence and assembly of segmental duplications. *Nat Methods* **16**: 88-94.

Vollger MR, Guitart X, Dishuck PC, Mercuri L, Harvey WT, Gershman A, Diekhans M, Sulovari A, Munson KM, Lewis AP et al. 2022. Segmental duplications and their variation in a complete human genome. *Science* **376**: eabj6965.

Wickham H. 2009. *ggplot2: Elegant Graphics for Data Analysis*. Springer-Verlag New York.

Wickham H, Seidel D. 2022. scales: Scale Functions for Visualization.

Yilmaz F, Gurusamy U, Mosley TJ, Hallast P, Kim K, Mostovoy Y, Purcell RH, Shaikh TH, Zwick ME, Kwok PY et al. 2023. High level of complexity and global diversity of the 3q29 locus revealed by optical mapping and long-read sequencing. *Genome Med* **15**: 35.

Zhu Y, Wu Y, Kim JI, Wang Z, Daaka Y, Nie Z. 2009. Arf GTPase-activating protein AGAP2 regulates focal adhesion kinase activity and focal adhesion remodeling. *J Biol Chem* **284**: 13489-13496.

Tables

Table 1. *AGAP* genes annotated in the human genome (Ensembl release 110).

Gene symbol	Ensembl ID	Genomic location (hg38)	Size	Karyotype band	Gene type	1:1 ortholog in mouse	1:1 ortholog in mouse lemur	Orthologs in Catarrhini Primates
AGAP1	ENSG00000157985	chr2:235,494,043-236,131,793	637,973	2q37.2	protein coding	Yes	Yes	Yes
AGAP2	ENSG00000135439	chr12:57,723,761-57,742,157	18,398	12q14.1	protein coding	Yes	Yes	Yes
AGAP3	ENSG00000133612	chr7:151,085,831-151,144,436	58,574	7q36.1	protein coding	Yes	Yes	Yes
AGAP4	ENSG00000188234	chr10:45,825,594-45,853,875	28,277	10q11.22	protein coding	No	No	Yes
AGAP5	ENSG00000172650	chr10:73,674,287-73,698,109	23,822	10q22.2	protein coding	No	No	Yes
AGAP6	ENSG00000204149	chr10:49,982,190-50,011,654	29,470	10q11.23	protein coding	No	No	Yes
AGAP7P	ENSG00000264204	chr10:46,109,621-46,131,358	21,738	10q11.22	pseudogene	No	No	NA
AGAP9	ENSG00000204172	chr10:47,501,854-47,523,638	21,786	10q11.22	protein coding	No	No	Yes
AGAP10P	ENSG00000230869	chr10:45,678,692-45,700,532	21,838	10q11.22	pseudogene	No	No	NA
AGAP11	ENSG00000261011	chr10:87,001,636-87,009,905	8,272	10q23.2	noncoding RNA	No	No	NA
AGAP12P	ENSG00000265018	chr10:48,009,873-48,031,640	21,763	10q11.22	pseudogene	No	No	NA
AGAP13P	ENSG00000243289	chr10:46,816,516-46,837,947	21,416	10q11.22	pseudogene	No	No	NA
AGAP14P	ENSG00000279058	chr10:46,337,224-46,358,714	21,497	10q11.22	pseudogene	No	No	NA

Table 2. Copy-number estimates in samples with alternative haplotypes.

Sample	**Population**	**Haplotypes**	***ANTXRL*** **(SUNK)**	***ANXA8*** **(WSSD)**	***GPRIN2*** **(WSSD)**	***NPY4R*** **(WSSD)**	***SYT15B*** **(WSSD)**	***PTPN20*** **(WSSD)**	***AGAP4*** **(WSSD)**
HG00735	AMR	H1, H4	2	5	5	5	5	4	19
HG01978	AMR	H5, H1	3	5	5	5	5	4	20
HG01361	AMR	H1, H6	3	6	6	6	6	4	23
HG00733	AMR	H7, NA	3	5	6	6	6	4	21
HG01358	AMR	H1, H8	2	4	4	4	4	4	19
HG01891	AFR	H1, H10	2	3	3	3	3	4	18
HG03540	AFR	H9, NA	2	4	4	4	4	4	18

Table 3. Features of rearrangements and breakpoints. The length and identity of the entire SD pair mediating the NAHR event as well as features of the narrowed breakpoint sequence are shown. Data were taken from the CAT + Liftoff Gene Annotations, RepeatMasker Repetitive Elements, and GC Percent in 5-Base Windows UCSC Genome Browser tracks (T2T-CHM13 v2.0).

Haplotype	Rearrangement		NAHR SD pair		Breakpoint				
	Class	Size (bp)	Length (kbp)	Identity (%)	Length (bp)	Identity (%)	Genes	Repetitive elements	GC content (%)
H2.1	Inversion	1,433,448	446	99.46	17,420	99.80	*NPY4R*	Large region	49
H2.2	Inversion	1,321,414	446	99.46	4,993	99.64	*AC244230.2*	Large region	48
H2.3	Inversion	1,510,974	446	99.46	4,999	99.84	*LINC00842*	Large region	52
H2.4	Inversion	993,568	446	99.46	25,598	99.89	*AL136982.3*	Large region	39
H2.5	Inversion	902,230	446	99.46	7,220	99.74	*FAM245B*	Large region	36
H3	Deletion	176,406	18	94.36	369	100	No	No	66
H5	Duplication	714,524	56	99.15	867	100	No	LINE L1M4	43
H9	Inversion	1,089,232	68	99.20	1,207	100	*ANXA8*	LINE L4_C_Mam	51
H10	Deletion	501,667	446	99.46	19,957	99.79	*FAM245B*	Large region	34
H11	Deletion	671,796	122	99.63	1,641	99.70	*FRMPD2*	LTR33+MER20	52

Figures and Figure Legends

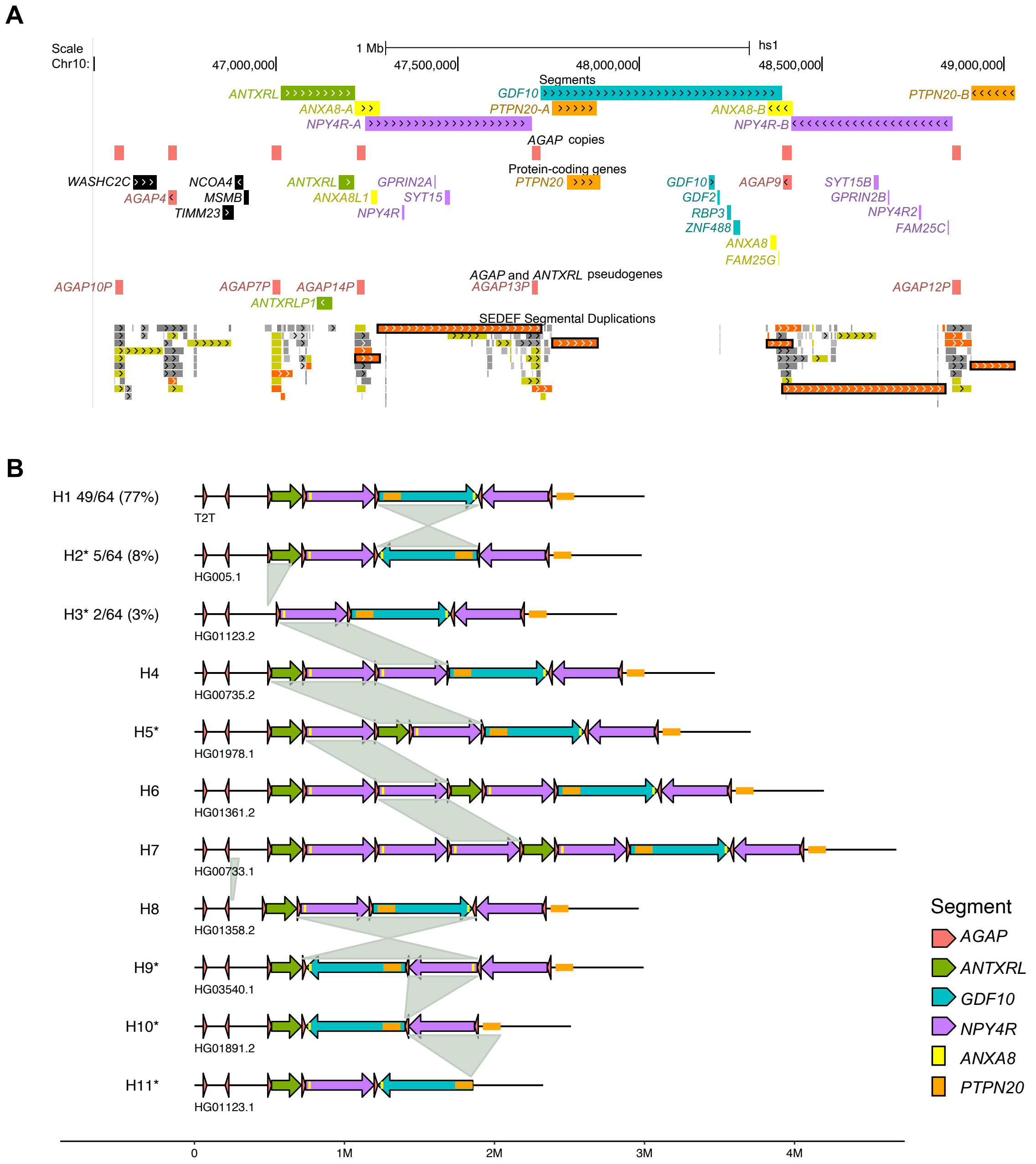

Figure 1. Structural variation at the 10q11.22 chromosomal region. A) Annotation of segments, genes, and SDs. View in the UCSC Genome Browser on human T2T-CHM13 v2.0 of the region Chr10:46,500,000-49,100,000. The following segments are drawn: *ANTXRL* (green), *NPY4R-A/B* (violet), *ANXA8-A/B* (yellow), *PTPN20-A/B* (orange), and *GDF10* (blue). *ANXA8-A* overlaps *NPY4R-A* while *ANXA8-B* is just outside the *NPY4R-B* segment. The location of *AGAP* copies (protein-coding genes and pseudogenes) is shown

with red boxes. Protein-coding genes and the *ANTXRL* pseudogene are indicated, with the text colored according to the segment they belong to. At the bottom, SD annotation with colors reflecting the level of similarity: light to dark grey for 90-98%; yellow for 98-99%; orange for similarity greater than 99% (Numanagic et al. 2018; Vollger et al. 2022). Black rectangles mark the three pairs of inverted SDs that overlap the *NPY4R*, *ANXA8*, and *PTPN20* segments, respectively. **B) Schematic of 11 alternative haplotypes identified in 64 haploid genomes**. Numbers next to H1, H2, and H3 haplotypes represent their frequency. All other haplotypes were identified in a single genome. H1 corresponds to the T2T-CHM13 haplotype and is the most common. Asterisks denote haplotypes validated by the GAVISUNK tool. Grey links between haplotypes highlight the underlying structural variation.

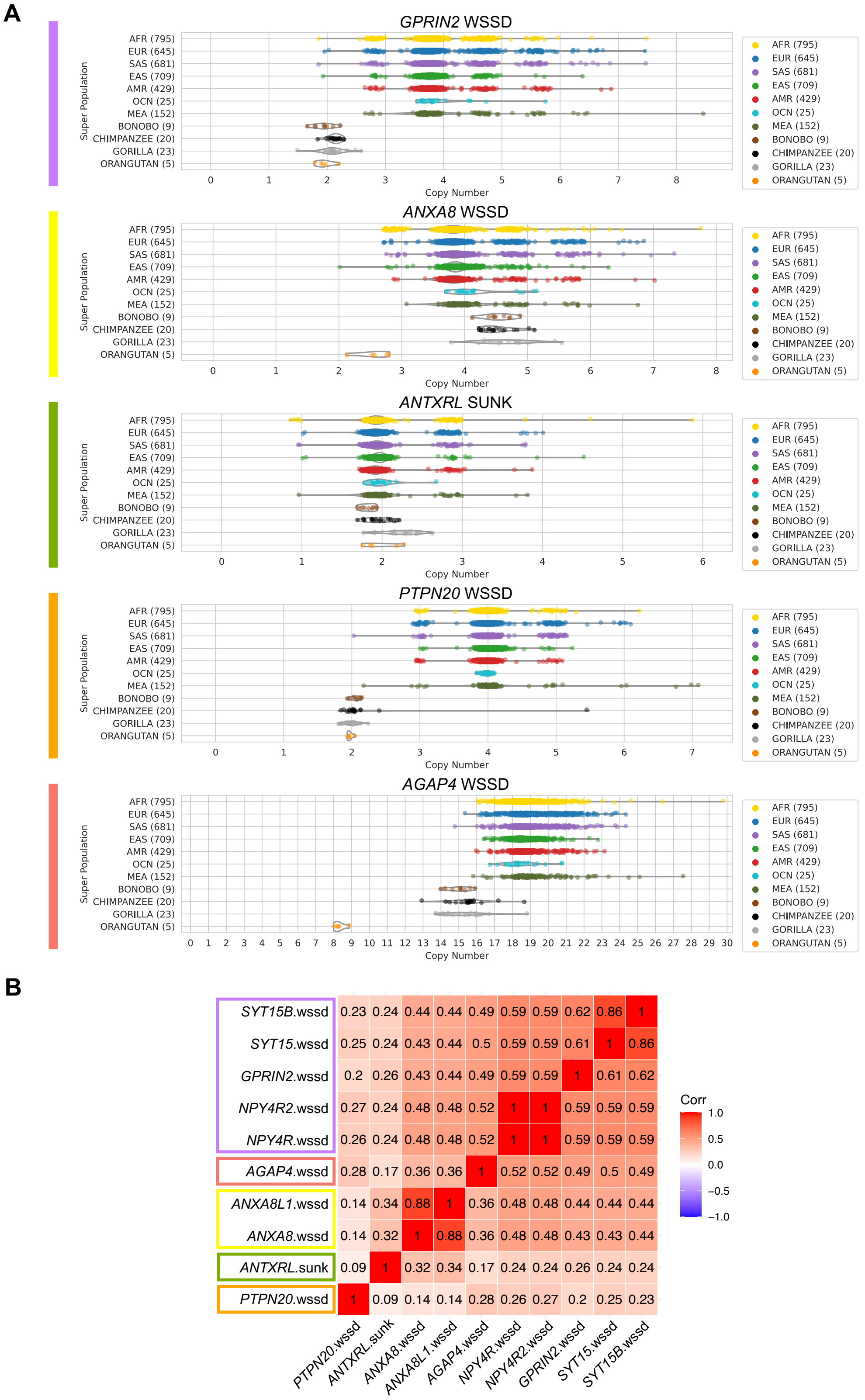

	PTPN20.wssd	ANTXRL.sunk	ANXA8.wssd	ANXA8L1.wssd	AGAP4.wssd	NPY4R.wssd	NPY4R2.wssd	GPRIN2.wssd	SYT15.wssd	SYT15B.wssd
SYT15B.wssd	0.23	0.24	0.44	0.44	0.49	0.59	0.59	0.62	0.86	1
SYT15.wssd	0.25	0.24	0.43	0.44	0.5	0.59	0.59	0.61	1	0.86
GPRIN2.wssd	0.2	0.26	0.43	0.44	0.49	0.59	0.59	1	0.61	0.62
NPY4R2.wssd	0.27	0.24	0.48	0.48	0.52	1	1	0.59	0.59	0.59
NPY4R.wssd	0.26	0.24	0.48	0.48	0.52	1	1	0.59	0.59	0.59
AGAP4.wssd	0.28	0.17	0.36	0.36	1	0.52	0.52	0.49	0.5	0.49
ANXA8L1.wssd	0.14	0.34	0.88	1	0.36	0.48	0.48	0.44	0.44	0.44
ANXA8.wssd	0.14	0.32	1	0.88	0.36	0.48	0.48	0.43	0.43	0.44
ANTXRL.sunk	0.09	1	0.32	0.34	0.17	0.24	0.24	0.26	0.24	0.24
PTPN20.wssd	1	0.09	0.14	0.14	0.28	0.26	0.27	0.2	0.25	0.23

Figure 2. Copy number of 10q11.22 genes. A) WSSD or SUNK estimates of *GPRIN2*, *ANXA8*, *ANTXRL*, *PTPN20*, and *AGAP4* copy number in 1KGP, HGDP, and nonhuman

primate panels. The color of the line to the left of each plot corresponds to the color code of the segment where the gene is located (see Fig. 1A). **B)** Spearman’s correlations between copy-number estimates of *NPY4R/R2*, *GPRIN2*, *SYT15/15B*, *AGAP4*, *ANXA8L1*, *ANXA8*, *ANTXRL*, and *PTPN20*. All values are significant. The color of rectangles around gene symbols corresponds to the color code of the segment where the genes are located (see Fig. 1A).

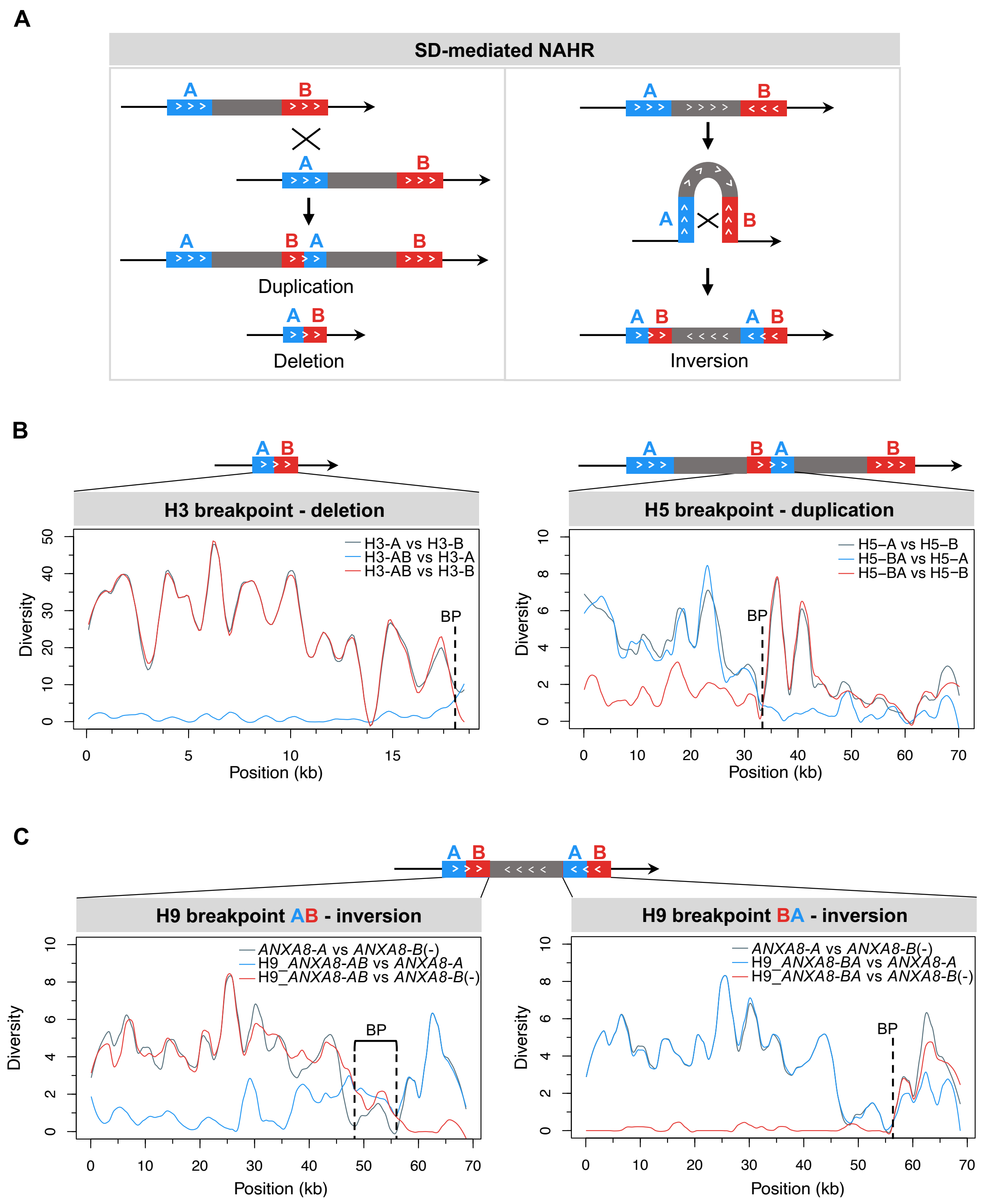

Figure 3. Characterization of rearrangement breakpoints in H3, H5, and H9 haplotypes. A) (*left*) Schematic of interchromosomal or interchromatid NAHR between directly oriented SDs resulting in reciprocal duplication and deletion. The misalignment of two directly oriented SDs—block A (blue) and block B (red)—produces two chromatids: one carrying a duplication and the other a deletion of the sequence between them (grey), as

well as of the SDs themselves. In the chromatid with the duplication, the new SD copy is a "chimera," with the first portion derived from the downstream SD (B, red) and the second portion from the upstream SD (A, blue). Conversely, in the chromatid with the deletion, the remaining SD copy is a "chimera," with the first portion derived from the upstream SD (A, blue) and the second portion derived from the downstream SD (B, red). The switch from A to B (or vice versa) corresponds to the exact NAHR site. **(*right*) Schematic of intrachromatid NAHR between SDs with inverted orientation generating an inversion.** The misalignment of two SDs with inverted orientation—block A (blue) and block B (red)—generates an inversion of the sequence between the SDs (grey), as well as two hybrid "AB" SDs, with each copy having an A-derived and a B-derived portion. The switch site between the A and B blocks depends on the position of the NAHR breakpoint. **B) Diversity plots of H3 and H5 breakpoint regions compared with the putative SDs mediating the deletion/duplication.** The plots show the sliding window pairwise diversity between the H3/H5 breakpoint regions (H3-AB, H5-BA) and the original "A" (blue line) or "B" (red line) SDs. The grey line refers to the comparison between the parental SDs (H3-A *versus* H3-B; H5-A *versus* H5-B), as a reference. The dashed line indicates the location of the breakpoint, which is the point where the derived hybrid SD copy switches similarity from one copy (H3-A or H5-B) to the other (H3-B or H5-A) of the original SDs. **C) Diversity plots of H9 breakpoint regions compared with the putative SDs mediating the inversion.** Diversity plots of the H9 *ANXA8-AB* duplicon (*left*) or H9 *ANXA8-BA* duplicon, reverse strand (*right*) compared with the H1 *ANXA8-A* (blue line) or *ANXA8-B* (red line) duplicons. The grey line refers to the comparison between H1 *ANXA8-A* and *ANXA8-B* duplicons, as a reference. Dotted lines designate the breakpoint region.

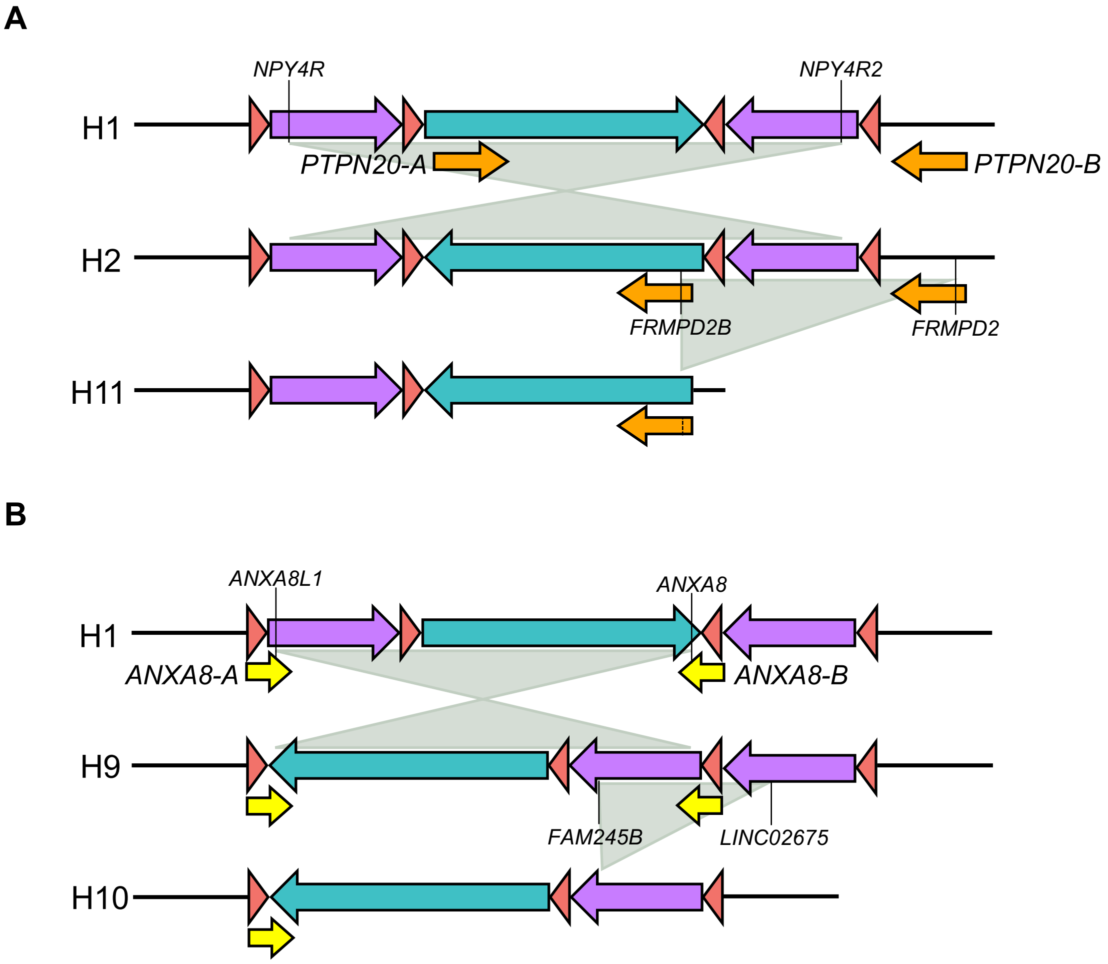

Figure 4. Inversion haplotypes generate new predispositions to copy-number variations. A) Schematic of H2 and H11 haplotypes. The H2 haplotype differs from H1 by an inversion mediated by *NPY4R* inverted duplicons (purple arrows). Following this inversion, the *PTPN20* duplicons (orange arrows) become in direct orientation and mediate the deletion identified in H11. Genes mapped at the breakpoints are specified. **B) Schematic of H9 and H10 haplotypes.** The H9 haplotype differs from H1 by an inversion mediated by *ANXA8* inverted duplicons (yellow arrows). Following this inversion, the *NPY4R* duplicons (purple arrows) become in tandem configuration and direct orientation and mediate the deletion of one copy in H10 haplotype. Genes mapped at the breakpoints are specified.

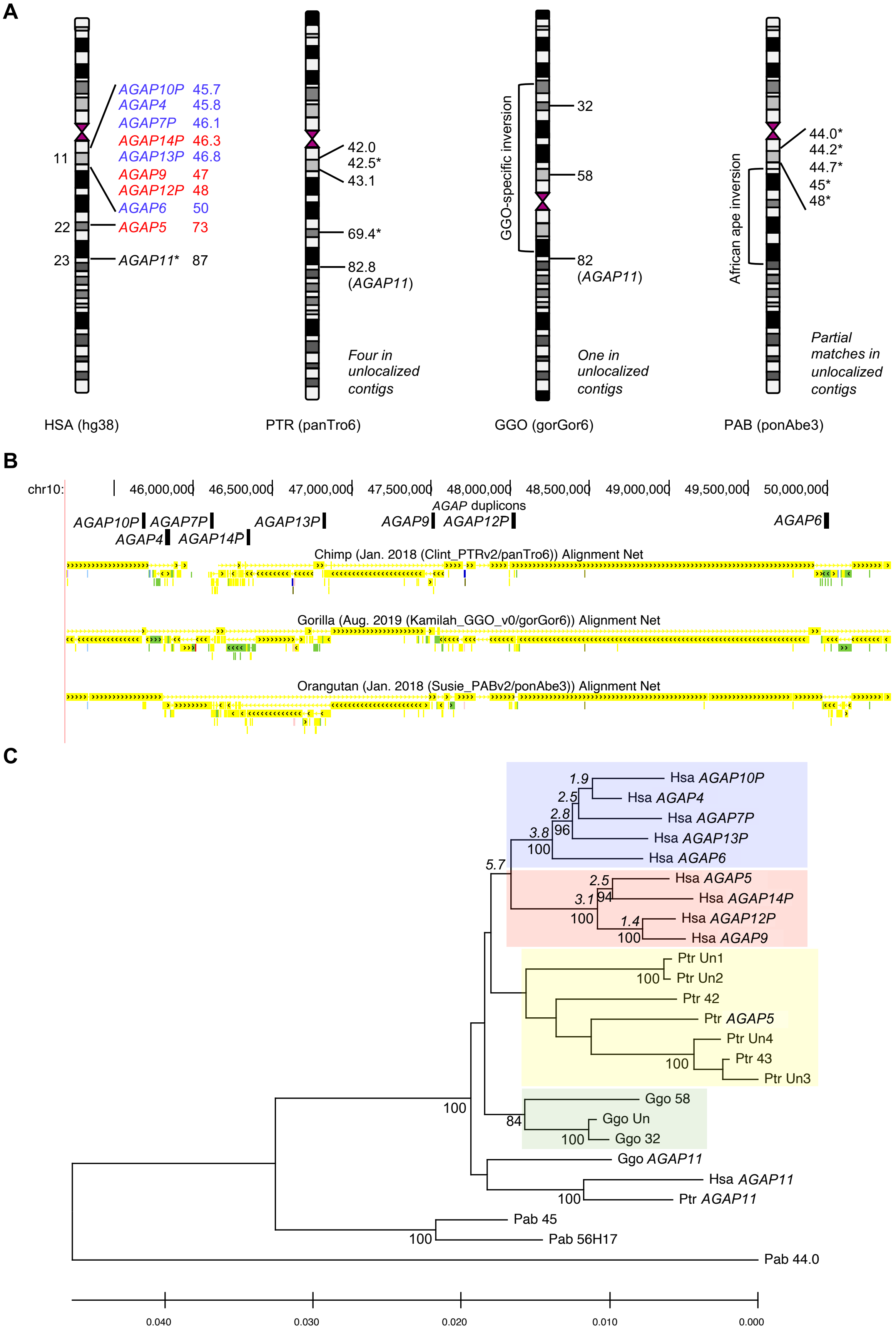
A
AGAP10P 45.7
AGAP4 45.8
AGAP7P 46.1
AGAP14P 46.3
AGAP13P 46.8
AGAP9 47
AGAP12P 48
AGAP6 50
AGAP5 73
AGAP11* 87
11
22
23
HSA (hg38)
42.0
42.5*
43.1
69.4*
82.8
(AGAP11)
Four in unlocalized contigs
PTR (panTro6)
GGO-specific inversion
32
58
82
(AGAP11)
One in unlocalized contigs
GGO (gorGor6)
African ape inversion
44.0*
44.2*
44.7*
45*
48*
Partial matches in unlocalized contigs
PAB (ponAbe3)
B
chr10:
46,000,000
46,500,000
47,000,000
47,500,000
48,000,000
48,500,000
49,000,000
49,500,000
50,000,000
AGAP duplicons
AGAP10P
AGAP7P
AGAP13P
AGAP9
AGAP12P
AGAP6
AGAP4
AGAP14P
Chimp (Jan. 2018 (Clint_PTRv2/panTro6)) Alignment Net
Gorilla (Aug. 2019 (Kamilah_GGO_v0/gorGor6)) Alignment Net
Orangutan (Jan. 2018 (Susie_PABv2/ponAbe3)) Alignment Net
C
1.9
Hsa AGAP10P
2.5
Hsa AGAP4
2.8
Hsa AGAP7P
3.8
96
Hsa AGAP13P
100
Hsa AGAP6
5.7
2.5
Hsa AGAP5
3.1
94
Hsa AGAP14P
100
1.4
Hsa AGAP12P
100
Hsa AGAP9
Ptr Un1
100
Ptr Un2
Ptr 42
Ptr AGAP5
Ptr Un4
Ptr 43
100
Ptr Un3
Ggo 58
84
Ggo Un
100
Ggo 32
100
Ggo AGAP11
Hsa AGAP11
100
Ptr AGAP11
Pab 45
100
Pab 56H17
Pab 44.0
0.040
0.030
0.020
0.010
0.000

Figure 5. Genomic organization and phylogeny of Chromosome 10 *AGAP* copies in great apes. A) Chromosome location (in Mbp) of *AGAP* copies in human, chimpanzee, gorilla, and orangutan reference genomes according to the most recent releases. In the common ancestor of African apes, a pericentric inversion moved *AGAP11* outside the pericentromeric region. Copies with an asterisk (*) are shorter than the others and are thus incomplete. Human *AGAP* copies are colored according to the clade in the phylogenetic tree shown in panel C. **B)** Pairwise genomic sequence alignments of the q-arm pericentromeric region of human Chromosome 10 with great ape genomes (UCSC track of primate net alignments). The location of *AGAP* duplicons is shown. **C)** Phylogeny of Chromosome 10 *AGAP* copies in great apes. The tree was inferred by using the Maximum Likelihood method and Kimura 2-parameter model. The tree is drawn to scale, with branch lengths measured in the number of substitutions per site. All positions containing gaps and missing data were eliminated (complete deletion option). There was a total of 4961 positions in the final dataset. Bootstrap values greater than 75 are shown next to significant nodes. Timing estimates in millions of years of split events between human *AGAP* copies are shown in italics.